Thermal atomic layer deposition of Sn metal using SnCl₄ and a vapor phase silyl dihydropyrazine reducing agent

Eric C. Stevens, Moataz Bellah M. Mousa, and Gregory N. Parsons

Citation: Journal of Vacuum Science & Technology A 36, 06A106 (2018); doi: 10.1116/1.5055212

View online: https://doi.org/10.1116/1.5055212

View Table of Contents: http://avs.scitation.org/toc/jva/36/6

Published by the American Vacuum Society





Thermal atomic layer deposition of Sn metal using SnCl₄ and a vapor phase silyl dihydropyrazine reducing agent

Eric C. Stevens,^{a)} Moataz Bellah M. Mousa,^{a)} and Gregory N. Parsons^{b)}
Department of Chemical and Biomolecular Engineering, North Carolina State University, 911 Partners Way, Raleigh, North Carolina 27695

(Received 6 September 2018; accepted 30 October 2018; published 20 November 2018)

This work explores a novel, thermal atomic layer deposition (ALD) process to deposit tin metal at a low temperature. The authors employ 1,4-bis(trimethylsilyl)-1,4-dihydropyrazine (DHP) to reduce SnCl₄ on silicon substrates. The authors explored a range of temperatures between 130 and 210 °C to determine the ALD window, which was found to be 170–210 °C. The authors show that this process yields a growth rate of ~0.3 Å per cycle at 190 °C. Furthermore, X-ray photoelectron spectroscopy results showed that the film impurities are reduced for depositions within the ALD window. The reaction mechanism was explored using *in situ* mass spectrometry and *in situ* quartz crystal microbalance (QCM). Within the ALD temperature window, the QCM results showed a saturated mass gain during the SnCl₄ exposure and a net mass loss during the DHP dose. Consistent with the QCM results, *in situ* mass spectroscopy data indicate that the DHP exposure step removes surface Cl via formation of volatile trimethylsilyl chloride and pyrazine by-products, effectively reducing the oxidation state of surface-bound Sn. This work is the first thermal Sn metal ALD process to be reported in literature and the oxidation/reduction chemistry presented here may be applied to other metal precursors, increasing the applicability of metal ALD use in industry. *Published by the AVS*. https://doi.org/10.1116/1.5055212

I. INTRODUCTION

Tin is an intriguing metal that boasts various applications spanning multiple fields. For example, Sn has been proposed as a candidate material for confinement modulated gap nanowire transistors. Electronic structure calculations suggest that when Sn is confined in nanowire structures less than 5 nm diameter, it undergoes a transition from semimetal to semiconductor, thereby providing an alternative approach to atomic scale transistor scaling.

Tin is also used as an anode for lithium ion batteries.³ Key advantages include an exceptionally high gravimetric capacity (959 mAh g⁻¹),⁴ a good electrical conductivity (9.17 × 10⁴ S cm⁻¹),³ and a high Li-ion diffusivity (5.9 × 10⁻⁷ cm² s⁻¹).⁵ The major drawback for Sn anodes is the large volume expansion (~225%) upon Li-ion insertion, leading to a loss of electrical contact and physical cracking.³ This drawback can be addressed by controlling the metal film thickness,⁶ nanostructure,⁷⁻⁹ and morphology.^{10,11} Typically, Sn films are deposited on anodes by either electroplating¹¹ or physical vapor deposition¹² but the increasing need for 3D battery architectures and porous anode scaffolds¹³ challenges the coating limits of these techniques. The ability to deposit conformal Sn thin films by a thermally driven atomic layer deposition (ALD) process could help address these limitations.

In this work, we investigate 1,4-bis(trimethylsilyl)-1,4-dihydropyrazine (DHP) as a vapor-phase reducing agent for Sn ALD from tin (IV) tetrachloride (SnCl₄). First synthesized by Saito *et al.*,¹⁴ DHP and its derivatives have been used for the salt-free reduction of chloride-containing transition metal

b)Electronic mail: gnp@ncsu.edu

complexes. Saito showed that DHP can reduce liquid phase transition metal complexes to a lower oxidation state, but did not explore their efficacy in reduction of vapor-phase species. 14 Klesko et al. 15 previously utilized DHP as a vaporphase reducing agent to reduce TiCl₄ to elemental Ti. We propose that DHP can also be used to form Sn metal films via a thermal ALD process at temperatures below the melting point of Sn (231.9 °C). 16 The hallmark ALD characteristics of precursor exposure saturation, saturated growth conditions versus number of cycles, and ALD temperature window were investigated. Deposited films were tested for thickness uniformity and film purity. As a key addition to the understanding of DHP-based metal ALD, we utilized in situ analysis tools to characterize the ALD half-reactions, allowing us to propose a detailed reaction sequence that is consistent with the resulting material properties.

II. EXPERIMENT

A. Reactor setup

All ALD experiments were conducted in a homemade, hot wall, reactor operating in the viscous flow regime. Figure 1 shows the reactor schematic. All reactor lines were resistively heated to at ~100 °C to prevent precursor condensation during the delivery process. The deposition chamber (~3.5 cm diameter 316 stainless-steel tube) was resistively heated using proportional–integral–derivative (PID) temperature controllers spanning. The maximum deposition temperature tested was 210 °C to avoid additional film morphology changes near melting point of bulk Sn at 231.9 °C. ¹⁶ The charge cell, indicated in Fig. 1, allowed for direct precursor charge into a known volume, where the pressure could be measured using a MKS Baratron capacitance manometer.

^{a)}E. C. Stevens and M. B. M. Mousa contributed equally to this work.

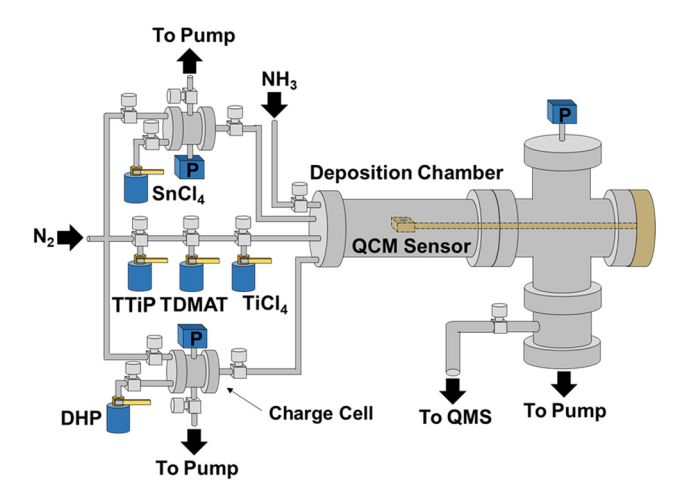


Fig. 1. Homemade, hot wall ALD reactor with direct-port and charge cell precursor delivery. N₂ carrier and purge gas were used, with an operating pressure of 1.5 Torr. *In situ* QCM and QMS capabilities were used to monitor the mass uptake and reaction by-products, respectively, during ALD processing.

The charge cell delivery allowed for consistent and controlled precursor exposures by continuously monitoring the precursor partial pressure. Dry and clean charge cell volumes were obtained by equipping each charge cell with a separate mechanical pump. The reactor also utilized *in situ* quartz crystal microbalance (QCM) and quadrupole mass spectrometry (QMS) capabilities to monitor the process during ALD processing. Research grade nitrogen (99.999%, Machine & Welding Supply Company) was further purified (Entegris Gate-Keeper) and used as the carrier and purge gas at an operating pressure of ~1.5 Torr.

B. ALD precursors and delivery

DHP was obtained from industry partners and was transferred, in a N_2 -filled glovebox, into a quartz bubbler vessel for ALD experiments. The bubbler was connected to the ALD reactor and, prior to initiation of ALD experiments, pumped down for \sim 5 min, at room temperature, to remove excess N_2 and ensure consistent dosing of DHP into the reactor chamber. The DHP bubbler was heated resistively and maintained at \sim 65–70 °C via a PID temperature controller to maintain a precursor pressure of \sim 1.3 Torr in the charge cell.

A typical DHP dosing sequence was performed as follows: (1) pumped down the charge cell until the pressure was below 100 mTorr, (2) closed pneumatic valve to charge cell pump, (3) charged DHP into charge cell for 3 s or until charge cell pressure read ~ 1.3 Torr, (4) closed DHP bottle and opened charge cell N_2 flow, (5) dosed DHP into deposition chamber for 3-5 s using the charge cell N_2 as the carrier gas, (6) purged deposition chamber and charge cell for 50 s with N_2 .

Tin (IV) chloride (SnCl₄) was purchased from Strem and used as received. SnCl₄ was selected as the metal precursor, because it has a suitable vapor pressure of 18.6 Torr at $20 \,^{\circ}\text{C}^{17}$ and a good thermal stability (up to at least $500 \,^{\circ}\text{C}$). The SnCl₄ vessel was not heated, but the delivery lines were kept at $\sim 100 \,^{\circ}\text{C}$. The dosing sequence for SnCl₄

also incorporated the charge cell delivery, as was used for the DHP, but with a 1 s precursor charge and 3 s dose into the deposition chamber.

For some experiments, deposited Sn layers were directly coated in the same deposition reactor with capping layers consisting of titanium nitride (TiN) followed by titanium dioxide (TiO₂) ALD at 190 °C. These layers were used to limit Sn surface oxidation and adventitious carbon contamination upon exposure to air. TiN and TiO₂ precursors were obtained from Strem and used as received. TiN was deposited directly on top of the Sn layer by tetrakis(dimethylamido)titanium (TDMAT) and NH3, with the TDMAT source temperature resistively heated to 45 °C with a dosing scheme of TDMAT/N₂/NH₃/ N_2 : 4 s/50 s/6 s/100 s. A TiO₂ film was then deposited using the titanium (IV) chloride (TiCl₄) and titanium tetraisopropoxide (TTiP), with the TTiP source temperature resistively heated to 80 °C, (TTiP/N₂/TiCl₄/N₂: 2 s/50 s/1 s/50 s). Based on our own analysis and previous reports of TiN¹⁹ and $TiO_2^{20,21}$ growth rates, we expect that 1300 cycles of TDMAT/NH₃ produced ~80 nm of TiN and 1500 cycles of TTiP/TiCl₄ led to ~45 nm of TiO₂ based on cross-sectional scanning electron microscope (SEM) measurements.

C. Substrate preparation

For ex situ analysis, films were deposited on silicon (100) (WRS Materials) with native oxide present, cut into 1 cm \times 1 cm pieces. For hydrogen terminated silicon (Si–H), the cut pieces of Si were dipped into a dilute HF solution (7% by volume) for 30 s and then rinsed with deionized water. For deposition, the substrates were placed on a stainless-steel sample holder, inserted into the reactor, and pumped down to the reactor base pressure (\sim 0.01 Torr). Before deposition began, the samples and sample holder were stabilized for 30 min in the reactor under dry N₂ flow at the operating pressure of 1.5 Torr and the desired deposition temperature, between 130 and 210 °C.

To inhibit film oxidation when removing the Si samples for *ex situ* analysis, a capping layer was deposited prior to removal of the samples. The capping layer consisted of two films. A TiN ALD film was deposited directly on the Sn film using TDMAT/NH₃ at 190 °C, followed by a TiO₂ ALD film using TiCl₄/TTiP at 190 °C. Due to previous reports²² of porosity for TiN films deposited below 200 °C, a waterless TiO₂ ALD process was used to fill the pores in the TiN film. Using ALD processes for pore filling has been well represented in the literature.^{23–26} The selection of TiO₂ specifically was due to the well-studied, waterless deposition process using readily available precursors in our lab.²⁰

For QCM analysis, Au-coated quartz crystals (Inficon, 6 MHz AT-cut quartz, 0.55" diameter, unpolished) were used as received.

D. In situ characterization

For QCM experiments, a commercial QCM assembly (Cool Drawer, Inficon) was specially modified to allow a constant flow of ~ 0.3 Torr of N_2 to purge the back side of

the quartz crystal. This modification prevented unwanted deposition during ALD processing on the electrode contacts. The modified QCM assembly was inserted into the ALD reactor, with the sensor head containing the QCM crystal positioned in the center of the deposition chamber. Before starting deposition runs, the QCM sensor was held in the reactor for $\sim 4-$ h under dry N_2 flow at the operating pressure of 1.5 Torr to allow the sensor to reach thermal equilibrium at the desired deposition temperature. Thermal equilibrium was reached after changes in steady-state QCM frequency were less than ~ 0.5 Hz over 30 min. Higher temperatures required longer equilibration times. Mass change measurements were recorded using an Inficon SQM-160 controller at a sampling rate of 10 Hz.

In situ mass spectrometry characterization relied on a MKS Vision 2000c QMS equipped with a triple-filtered quadrupole with a mass range of 1–300 amu. Sampled gases were ionized using a commercially available thoriated iridium filament and detected using an electron multiplier (referenced against a Faraday cup detector) with a gain of 100. The calibration of the ionized gas partial pressures was performed with a capacitance manometer.

To maximize the conductance of gaseous species during sampling, the lines connecting the reactor exhaust to the QMS inlet had an outside diameter of 2.75 in. Additionally, these lines were maintained at $\sim 100~^{\circ}$ C to prevent undesired precursor condensation and maintain effective purging. Furthermore, the QMS sampling volume was heated to 85 $^{\circ}$ C. The reported mass fragments for the reactants and products were identified with the aid of NIST mass spectrometry database. ²⁷

For direct sampling of the unreacted $SnCl_4$ and DHP molecules, the data were collected by directly connecting the QMS to the respective precursor charge cell. Charge cell temperatures were maintained at 120 °C to prevent undesired precursor contamination during charge sequences. Prior to collecting data, $SnCl_4$ or DHP were pulsed directly through the QMS system for at least 50, 1 s subdoses, separated by 5 s N_2 purges. This method was used such that the resulting spectra should represent characteristic ion fragments for each precursor in the unreacted state. Data were then collected continuously from m/z = 20-240 during precursor subdoses.

To monitor the reactants and products during SnCl₄/DHP processing, the QMS was connected to the outlet of the reactor so that all exhaust gas passed through the sampling chamber before going to the rotary vacuum pump. Prior to collecting data, at least 200 cycles of SnCl₄ and DHP were used to condition the reactor walls.

E. Ex situ characterization

Cross-sectional SEM images were taken of the Si/Sn/TiN/TiO₂ samples using focused ion beam (FIB) and a FEI Verios 460L SEM. For the FIB processing, a $25 \,\mu\text{m} \times 2 \,\mu\text{m} \times 2 \,\mu\text{m}$ bar of platinum was deposited while the sample was inside the FIB SEM chamber to protect the area of interest from destruction during the ion milling process. After the milled channels were prepared in the FIB, the samples were transferred to the Verios SEM for high resolution cross-sectional imaging.

Compositional analysis was performed using a SPECS X-ray photoelectron spectroscopy (XPS) system with a PHOIBOS 150 analyzer. An Al Kα X-ray source operated at 400 W was used to generate the X-ray beam and Ar ions were used for the sputtering through the deposited layers. The gathered data was shifted accordingly by referencing the adventitious carbon peak (C 1s) to 284.8 eV. CasaXPS software was used to plot the spectra and determine the elemental concentrations. The NIST XPS database²⁸ was used for peak identification. Sn film composition was also characterized using time of flight secondary ion mass spectrometry (ToF-SIMS) on a TOF.SIMS5 (ION TOF, Inc. Chestnut Ridge, NY). The ToF-SIMS instrument utilized a 10 nA, 1 KeV Cs⁺ ion for depth profiling over a $200 \times 200 \,\mu\text{m}^2$ area. Film analysis used a 0.2 pA Bi₃⁺ primary ion beam to analyze a $50 \times 50 \,\mu\text{m}^2$ area within the sputtered region.

III. RESULTS AND DISCUSSION

A. Quartz crystal microbalance

Figure 2 shows the resulting mass change during SnCl₄/DHP exposures on untreated, Au-coated QCM crystals using $SnCl_4/N_2/DHP/N_2$ exposure times of 2 s/40 s/2 s/40 s, respectively at (a) 130 °C and (b) 170 °C. For depositions at 130 °C, the average mass uptake per cycle was nonlinear for the first 500 cycles, indicative of a nucleation delay. After approximately 500 cycles, the average mass change increased to $\sim 1000 \,\mathrm{ng}\,\mathrm{cm}^{-2}\,\mathrm{cycle}^{-1}$ and was linear for the remaining cycles. The inset in Fig. 2(a) shows three cycles of SnCl₄/ DHP at 130 °C, with the individual dose indicated by an arrow, within the region where the mass change per cycle was shown to be linear. The SnCl₄ dose resulted in a mass gain, while the DHP dose resulted in a mass loss. As discussed below, the large mass change at 130 °C corresponds to film growth outside the ALD temperature window. Furthermore, a mass loss and a mass gain were observed during purge steps after SnCl₄ and DHP dosing, respectively, also likely due to unsaturated surface reactions, and slow desorption of by-products, below the ALD temperature window.

For depositions at 170 °C, growth incubation on Au proceeded over the first 200 cycles, followed by linear mass uptake of ~200 ng cm⁻² cycle⁻¹. The inset in Fig. 2(b) shows three cycles of SnCl₄/DHP at 170 °C, within the region where the mass change per cycle was linear. Similar to that observed at 130 °C, SnCl₄ dosing resulted in a mass gain, while DHP dosing resulted in a mass loss.

Figure 3 shows other QCM results collected at 150 and 210 °C. Prior to recording these data, the Au-coated QCM substrates were exposed to at least 500 (at 150 °C) and 200 (at 210 °C) cycles of SnCl₄/DHP to reduce the potential impacts of film nucleation. The data show the mass change using multiple, consecutive 2 s subdoses of SnCl₄ or DHP, where each subdose was followed by 100 s (for 150 °C) or 200 s (for 210 °C) N₂ purges. Other data (not shown) confirm that similar trends were observed for purge times close to 40 s between doses.

Figure 3(a) shows five total SnCl₄/DHP cycles, with each cycle consisting of 10 (at 150 °C) and 5 (at 210 °C)

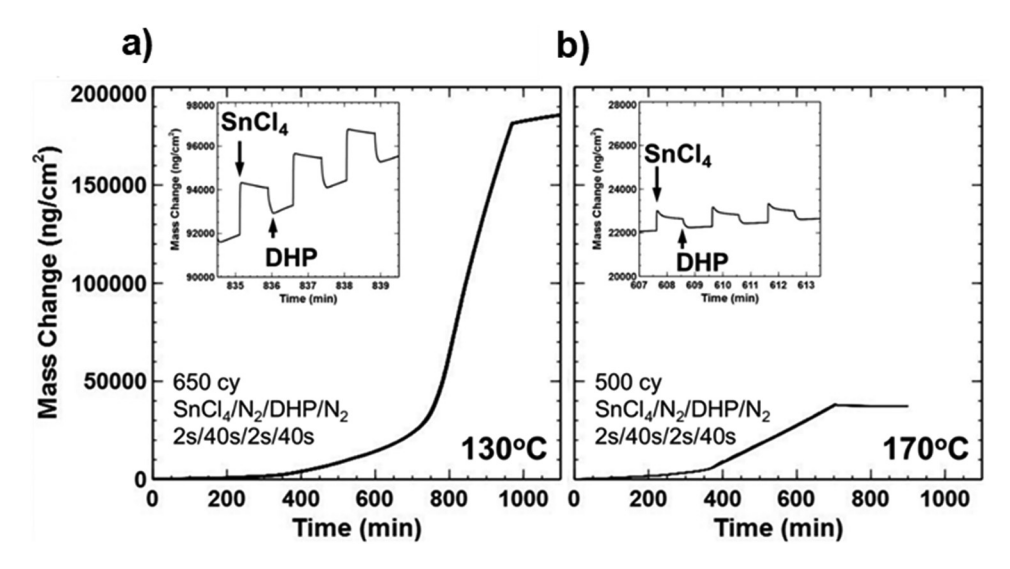


Fig. 2. Mass change, measured by QCM, as a function of deposition time during $SnCl_4/N_2/DHP/N_2$ (2 s/40 s) processing at (a) 130 °C for 650 cycles and (b) 170 °C for 500 cycles. Depositions were carried out on as-received Au-coated QCM crystals. Inset graphs show 3 cycles of $SnCl_4/N_2/DHP/N_2$ within linear mass uptake regions, with solid arrows indicating $SnCl_4$ and DHP dosing.

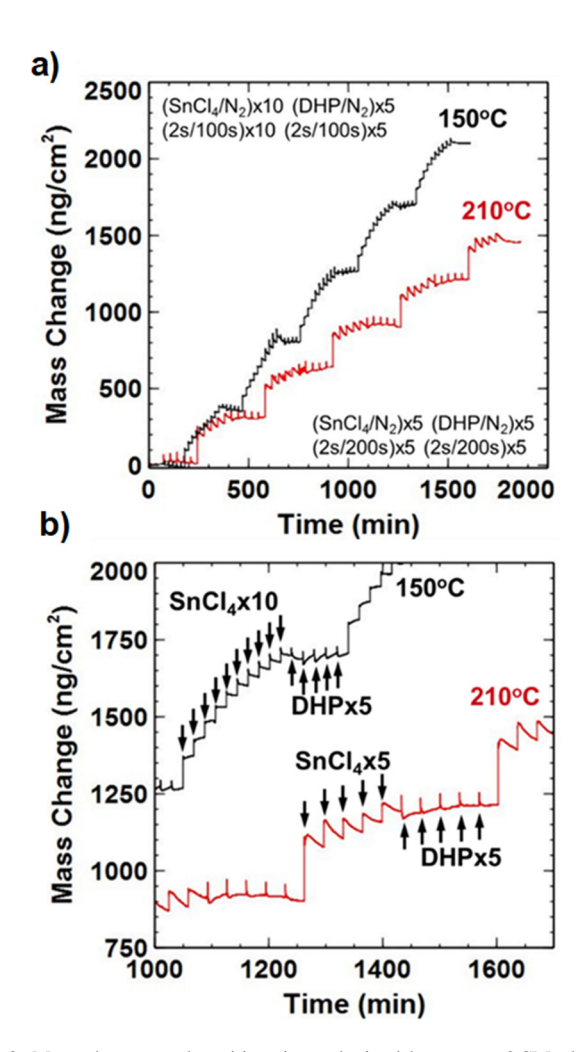


Fig. 3. Mass change vs deposition time, obtained by *in situ* QCM, during multiple consecutive SnCl₄/DHP exposures as a function of the deposition temperature, 150 (top, black line) and 210 °C (bottom, red line). (b) Magnified region from (a) to show subdose behavior. Solid arrows indicate the instance of 2 s SnCl₄ and DHP doses, separated by 100 and 200 s N_2 purges for depositions carried out at 150 and 210 °C, respectively.

consecutive SnCl₄ subdoses, followed by five consecutive DHP subdoses. Figure 3(b) shows a magnified region from Fig. 3(a), where SnCl₄ and DHP subdoses are indicated with arrows. At 150 °C, the first SnCl₄ subdose resulted in ~25% of the total mass gain measured for all 10 SnCl₄ subdoses, with ~80% of the total mass gain occurring after seven SnCl₄ subdoses. The first DHP subdose resulted in ~70% of the total mass decrease for all 5 DHP subdoses. The average mass change per cycle for 10 SnCl₄ and five DHP subdoses at $150 \,^{\circ}$ C was $430 \pm 50 \,\text{ng cm}^{-2} \,\text{cycle}^{-1}$. The data in Fig. 3 also show that for growth at 210 °C, the mass gain during the SnCl₄ subdoses produces saturation behavior, with >90% of the mass gain occurring within the first two SnCl₄ subdose. Likewise, for the DHP doses, the first DHP subdose resulted in ~95% of the total mass decrease. The average mass change per cycle at 210 °C for five SnCl₄ and five DHP subdoses was $250 \pm 10 \text{ ng cm}^{-2} \text{ cycle}^{-1}$.

Figure 4 shows the net mass change determined by QCM (after nucleation on Au-coated crystals) plotted versus deposition temperature. In the QCM data, saturation was specified when mass change during SnCl₄ and DHP subdoses reached >95% of the total mass change. For temperatures between 170 and 210 °C, saturation was observed in both half-reactions, with a net mass change ~250 ng cm⁻² cycle⁻¹ independent of temperature. For these tests, deposition was performed at least twice at each temperature, and error bars represent the standard deviation in the average growth rate obtained from separate runs. For T < 170 °C, we observed a net higher growth rate and more significant run-to-run variance.

B. Growth on QCM substrates

The expected growth per cycle (GPC) can be estimated using the mass uptake values from QCM analysis, coupled with the expected bulk density of Sn ($\rho_{\text{Sn}} = 7.3 \text{ g cm}^{-3}$). The GPC can then be compared to the expected thickness of one Sn monolayer, t_m , which is obtained from the Sn molecular

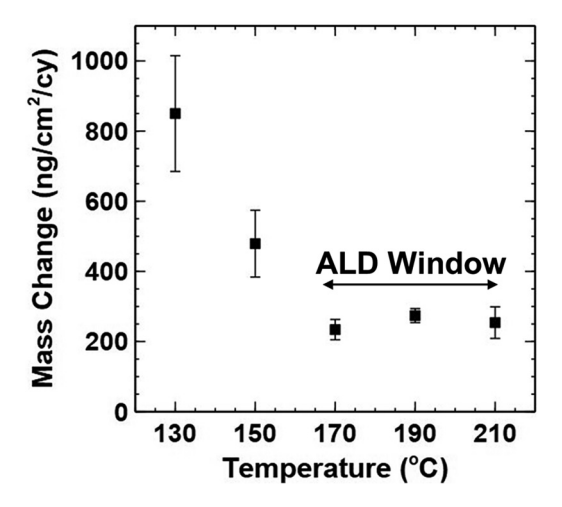


Fig. 4. Mass change, obtained by QCM, showing the average mass uptake per cycle obtained during SnCl₄/DHP depositions at 130, 150, 170, 190, 210 °C. The reported mass change is an average of the values obtained with saturated consecutive exposures, at a given temperature.

weight, $MW_{Sn} = 118.71 \text{ g mol}^{-1}$, and Avagadro's number, $N_A = 6.022 \times 10^{23} \text{ molecules mol}^{-1}$, as shown in Eq. (1),

$$t_m = \left[\frac{\text{MW}_{\text{Sn}}}{N_A \times \rho_{\text{Sn}}} \right]^{1/3}. \tag{1}$$

The mass change of $\sim 250 \, \mathrm{nm \, cm^{-2} \, cycle^{-1}}$ corresponds to $\sim 2.7 \, \mathrm{\mathring{A} \, cycle^{-1}}$. Since the bulk Sn monolayer thickness is $\sim 3 \, \mathrm{\mathring{A}}$, the observed steady-state mass uptake corresponds to $\sim 0.9 \, \mathrm{monolayer \, cycle^{-1}}$.

C. Film morphology on QCM and Si substrates

The films deposited on Au-coated QCM substrates were analyzed by SEM, and the images are shown in Fig. 5. Figure 5(a) shows an as-received, Au-coated QCM crystal, and (b) and (c) show the resulting films after 1000 cycles of the SnCl₄/DHP sequence at 150 °C and 190 °C, respectively.

For depositions at both temperatures, the resulting films were continuous and appear to conform to the rough QCM substrate. At 150 °C, particles with diameter of several hundred nanometers are observed distributed across the surface, with a broad distribution of particle size. Conversely, for depositions performed at 190 °C, the surfaces appeared smooth, without large visible particles.

The deposited films were also characterized using cross-sectional SEM imaging, as shown in Fig. 6. For these samples, the metal deposition was performed on hydrogenterminated silicon wafers. In the same reactor, a capping layer was then deposited, consisting of ALD TiN followed by ALD TiO₂ using conditions described in Sec. II. The aforementioned film stack is denoted as Si-H/Sn/TiN/TiO₂.

In Fig. 6, the Sn layer was deposited using 1500 cycles of SnCl₄/DHP at 190 °C. Figure 6(a) shows good film uniformity of the deposited Sn layer within the $\sim 1 \,\mu$ m lateral scale of the image. Magnified images in Fig. 6(b) show that 1500 cycles lead to a Sn metal thickness of 41 ± 1 nm. Based

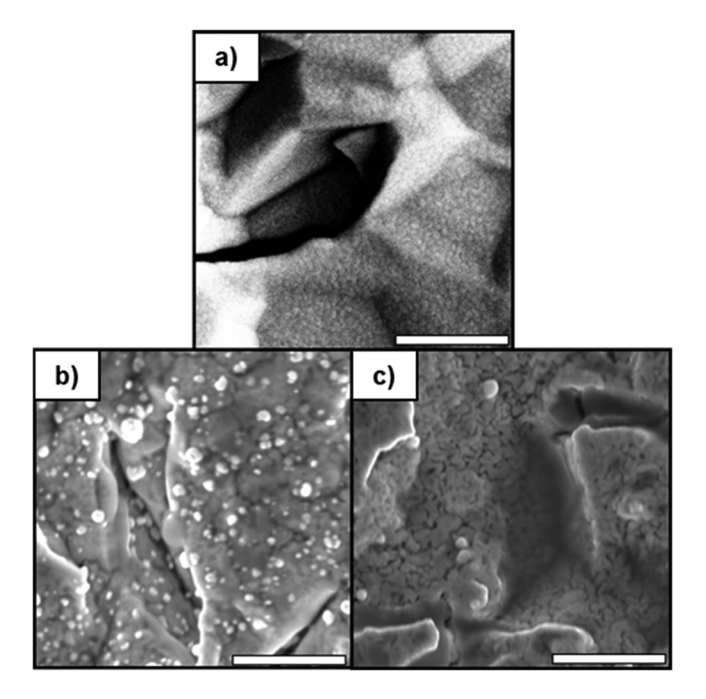


Fig. 5. Top-down SEM images of (a) as-received Au-coated QCM crystal, (b) 1000 cycles of SnCl₄/DHP deposited at 150 °C on Au-coated QCM crystal, (c) 1000 cycles of SnCl₄/DHP deposited at 190 °C on Au-coated QCM crystal. Scale bars are all $2\,\mu m$.

on the expected steady-state growth rate of ~3 Å cycle⁻¹, the observed thickness suggests that on the Si-H surface, a long incubation period (>1000 cycles) was needed before achieving steady-state growth.

In Fig. 6(b), it is noteworthy that the TiO₂ and the TiN layers were not discernable from one another via cross-sectional SEM, probably due to interlayer mixing. The Pt bar was used as a reference, as well as to protect the imaged sample area during ion milling.

D. Film composition

In order to better understand the quality of the deposited films, samples from the same run as that shown in Fig. 6 (without the Pt overcoat) were used for ToF-SIMS and XPS analysis. Films without a capping layer were also deposited and analyzed with XPS depth profiling, but showed SnO_x throughout the film (data not shown), indicating film oxidation after vacuum break. Therefore, a capping layer was used to better understand the chemical composition of the as-deposited films.

1. ToF-SIMS depth profiling

Figure 7 shows the secondary ion counts, obtained via ToF-SIMS, revealing an estimate of the species present within deposited film stack. Figure 7(a) shows four distinct layers present in the sample.

The first layer, measured during the first $\sim 100-150\,\mathrm{s}$ of sputtering, is ascribed to TiO₂, as evidenced by TiO₂, O₂, and $^{37}\text{Cl}^-$ ions from the TiCl₄/H₂O reagents. A decrease in $^{37}\text{Cl}^-$ signal near 150 s, coupled with a rise in CN⁻ is

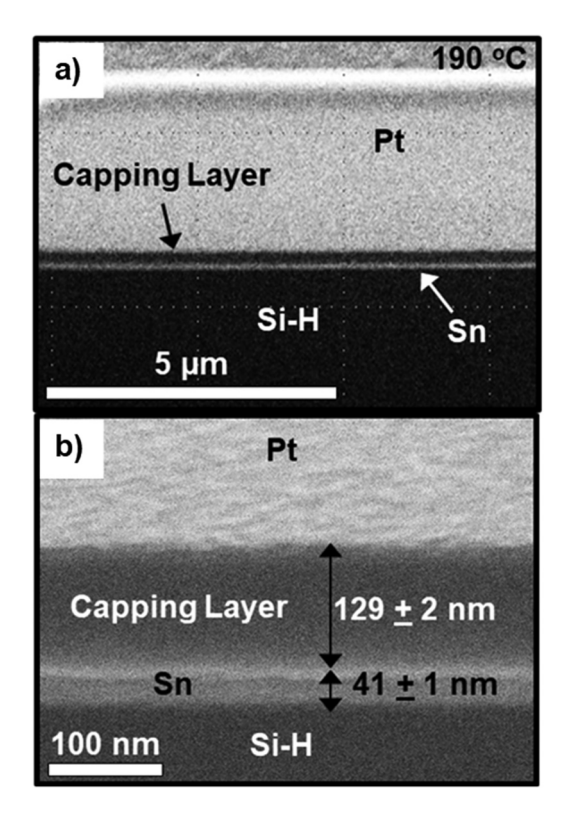


Fig. 6. (a) Cross-sectional SEM image of the Si-H/Sn/TiN/TiO $_2$ sample deposited at 190 °C (1500 cycles SnCl $_4$ /DHP, 1300 cycles TDMAT/NH $_3$, 1500 cycles TTiP/TiCl $_4$) and cut using a focused ion beam. The platinum bar was used to protective the area of interest during ion milling. Sn films show good thickness uniformity over the micrometer length scales. (b) Magnified SEM image of (a). The average thickness of the Sn layer was 41 ± 1 nm and the total (TiN + TiO $_2$) capping layer thickness was 129 ± 2 nm.

attributed to a transition from TiO₂ to TiN, where the CN⁻ originated from the amino ligands on the TDMAT precursor.

A third layer between 225 and 300 s corresponds to the deposited Sn, indicated by the Sn⁻ ions. Some overlap

between the Sn and TiN layer is likely due to the porosity of the TiN films. The Sn ion intensity reaches a maximum after $\sim\!240\,\mathrm{s}$ and remains nearly constant until about $300\,\mathrm{s}$. The substrate silicon layer is observed by the rise of Si^{2-} secondary ions coupled with the decrease in Sn^- .

Figure 7(b) shows the ion counts for potential impurities $(SnO_2^-, CN^-, and ^{37}Cl^-)$ within the Sn layer. The SnO_2^- intensity tracks well with the SiO_2^- signal, reaching a maximum near the Sn/Si interface. The CN^- and $^{37}Cl^-$ ion intensities are also large near the Sn/Si interface and decrease near the Sn/capping layer interface.

2. XPS depth profiling

Figure 8 shows the XPS spectra as a function of Ar sputtering time for *in situ* capped Sn samples deposited at 190 °C (i.e., same as in Figs. 6 and 7). Note that the Ar sputter rate during XPS in Fig. 7 is much slower than during ToF-SIMS in Fig. 7. After 20 min of sputtering in the XPS system to remove adventitious carbon, the survey scans in Fig. 8(a) show no discernable Cl 1s signal.

Ti 2p and O 1s peaks were observed at 459 and 531 eV, respectively, which corresponded with the TiO_2 portion of the capping layer. After 120 min of sputtering, Sn 3d peaks emerged in the region between 494 and 485 eV. These peaks were observed during all sputter times analyzed (up to 159 min), reaching an apparent maximum around 125–130 min.

After 159 min of sputtering, the increasing intensity of the Si 2p peak at 150 eV is indicative of the Sn/Si interface. The small peaks around 319 and 243 eV were assigned to Ar 1s and 2p, respectively, due to ion implantation during the sputtering process. The presence of Sn 3d peaks between 120 and 159 min sputtering gives the approximate bounds of the Sn layer. The Ti 2p and O 1s peaks in each spectrum in Fig. 8 are ascribed to a measurement artifact, where the XPS

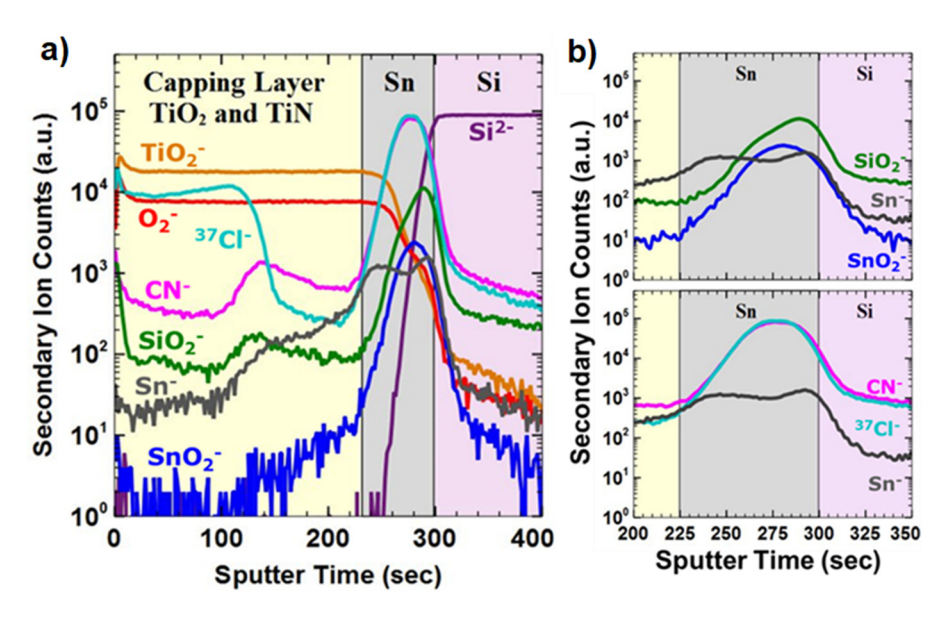


Fig. 7. (a) ToF-SIMS results of the Si-H/Sn/TiN/TiO₂ sample used for FIB SEM. Layers were labeled and color coded as follows: "Capping Layer TiO₂ and TiN"—yellow, "Sn"—grey, "Si"—purple. The ions tracked for the capping layer were TiO_2^- (orange), O_2^- (red), $^{37}Cl^-$ (teal), and CN^- (pink). The Sn^- (grey), SiO_2^- (green), and SnO_2^- (blue) were used to identify the Sn^- region. (b) O, C, N, and Cl impurities within the Sn^- region.

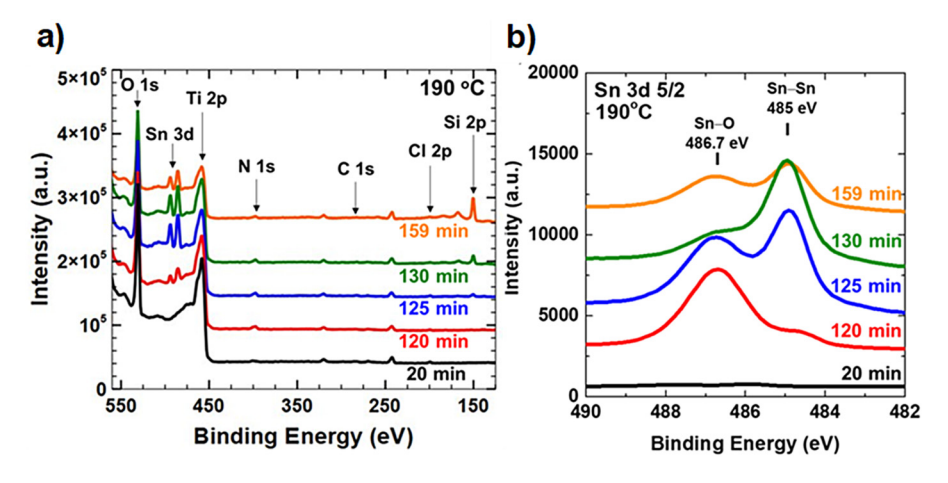


Fig. 8. (a) XPS survey scans of the Si-H/Sn/TiN/TiO₂ stack deposited at 190 °C. Each line represents the resulting survey scan of the same sample after 20–159 min Ar sputtering. After roughly 120 min of sputtering (red line), the Sn 3d peaks between 500 and 480 eV start to increase in intensity. A maximum in the Sn 3d peak intensity most likely occurs between 125 and 159 min of sputtering. After 159 min of sputtering, the Sn 3d peak intensity decreases accompanied with a rise Si 2p peak intensity, indicative of the underlying Si substrate. (b) High resolution scans of the Sn 3d 5/2 region showing Sn–Sn (485 eV) and Sn–O (486.7 eV) chemical bonds as a function of Ar sputter time of the same samples in (a). Spectra offset for visual clarity.

analysis probed a small region of the ${\rm TiO_2}$ cap layer that was not sputtered.

High resolution scans of the Sn 3d, N 1s, C 1s, and Cl 2p regions were performed to obtain elemental concentrations within the Sn layer. Figure 8(b) shows the Sn 3d 5/2 region where Sn–Sn and Sn–O bonds were identified at binding energies of 485 and 486.7 eV, respectively. After 20 min of sputtering, Sn 3d peaks were not discernable due to the capping layer. Sn 3d was visible after 120 min, primarily as Sn–O. After 130 min, the Sn–O peak intensity decreased, and a clear Sn–Sn peak becomes visible, with a maximum Sn–Sn/Sn–O ratio at 130 min. After sputtering 159 min, the ratio of the Sn–Sn/Sn–O peak area decreases, consistent with a SnO_x region at the SiO_x/Sn interface.

Quantification of C, Cl, and N impurities was accomplished using high resolution scans of the C 1s, Cl 2p, and N 1s after 130 min sputtering. Table I shows the resulting impurity content determined by XPS for films deposited at 130 °C and 190 °C. The peak area and relative sensitivity factor were considered when calculating the impurity percentages using CasaXPS software. At 130 °C, the Sn film contained 5 at. % C, 13 at. % Cl, and 9 at. % N impurities. Conversely, at 190 °C, those impurities decreased to 3 at. % C, 2 at. % Cl, and 4 at. % N. The atomic percent of oxygen in the Sn layer could not be determined unambiguously due to the oxygen present in the capping layer.

Table I. Film impurity content from XPS analysis vs deposition temperature.

Element	Impurity content (at. %)	
	130 °C	190 °C
Cl	13 ± 2.0	2 ± 0.4
N	9 ± 1.5	4 ± 0.5
С	5 ± 1.2	3 ± 0.4

E. *In situ* reaction monitoring by quadrupole mass spectrometry

In situ QMS was utilized to better understand the half-reactions during SnCl₄ and DHP exposures. For these experiments, the reactor temperature was set at 190 °C, and reactant dose sequences were described in Sec. II.

1. Characteristic mass fragments of unreacted SnCl₄ and DHP

Figures 9(a) and 9(b) show mass fragmentation patterns for $SnCl_4$ and DHP, respectively, collected by the mass spectrometer under constant reactant dosing into the deposition chamber. For these data, the QMS sensor was placed adjacent to the gas sources, leading to relatively large mass signals. In Fig. 9(a), the largest peak was observed at m/z = 224, ascribed to $SnCl_3^+$, an expected electron impact fragment of $SnCl_4$. Likewise, in Fig. 9(b), the most prominent peak occurs at m/z = 146. The detection of this mass fragment is likely due to subsequent reactions of species after chemical cracking from the QMS filament. An m/z of 146 was consistent with ionized hexamethyl disilane.

Potential reaction by-products produced during the $SnCl_4/DHP$ reaction include TMS-Cl and pyrazine. From the NIST mass spectroscopy database, ²⁷ TMS-Cl is expected to give peaks at m/z = 65, 73, 74, 77, 93, and 95, and pyrazine at m/z = 53 and 80. However, as shown in Fig. 9(b), the parent DHP gives peaks at these same mass values. To maintain favorable signal amplitude and avoid overlap with other expected reactants or by-products, we choose the peaks at m/z = 224 and 146 to monitor $SnCl_4$ and DHP species, respectively,

2. In situ reaction analysis during SnCl₄/DHP processing

Figure 10 shows the measured partial pressure at m/z = 224 and 146 as a function of time, collected downstream from the deposition zone during steady-state deposition at 190 °C

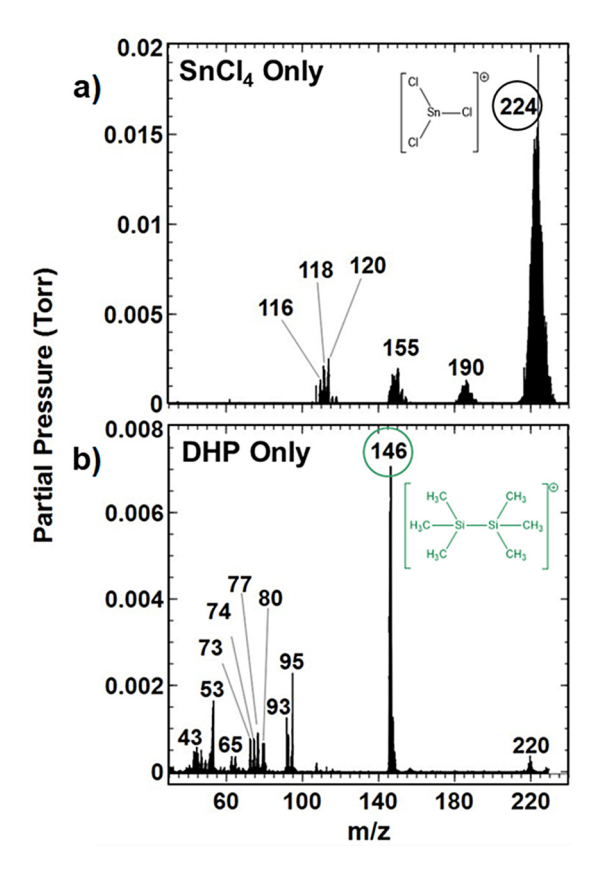


Fig. 9. Analog mass spectrometry scans from direct sampling of each individual charge cell (maintained at $120\,^{\circ}$ C), and thus the unreacted SnCl₄ and DHP species. (a) SnCl₄ mass fragmentation patterns for 50 consecutive doses, separated by N₂ purges. Most prominent peak observed at m/z = 224, with predicted structure of the SnCl₄ mass fragment shown. (b) DHP mass fragmentation patterns for 50 consecutive doses, separated by N₂ purges. Most prominent peak observed at m/z = 146, with predicted structure of the DHP mass fragment shown.

using five subdoses of each SnCl₄ and DHP, separated by N₂ purges. The dosing sequence is shown in Fig. 10(c). In Fig. 10(a), the first SnCl₄ subdose produces no measurable SnCl₄ signal at m/z = 224. During the following subdoses, a peak appears and increases to saturation during the third subdose. Also, during the SnCl₄ dose period, Fig. 10(a) shows no detectable signals for DHP at m/z = 146, and no other DHP peaks were observed.

During the subsequent DHP subdoses, Fig. 10(b) shows a signal at m/z = 146 during the first subdose, followed by a less intense signal that saturates during the second to fifth subdoses. The intensity of the m/z = 146 peak during saturation is smaller than that in Fig. 9 due to the downstream measurement configuration. During DHP subdosing, no signal was observed related to SnCl₄ fragments. The peak during the first DHP subdose is ascribed to TMS-Cl formed upon DHP abstraction of surface chlorine, and the saturation in the DHP signal corresponds to completed DHP reaction. Since the m/z = 146 peaks were larger with the first dose, followed by saturated behavior, the formation of TMS-Cl likely facilitates additional formation of hexamethyl disilane downstream during chemical cracking at the QMS filament.

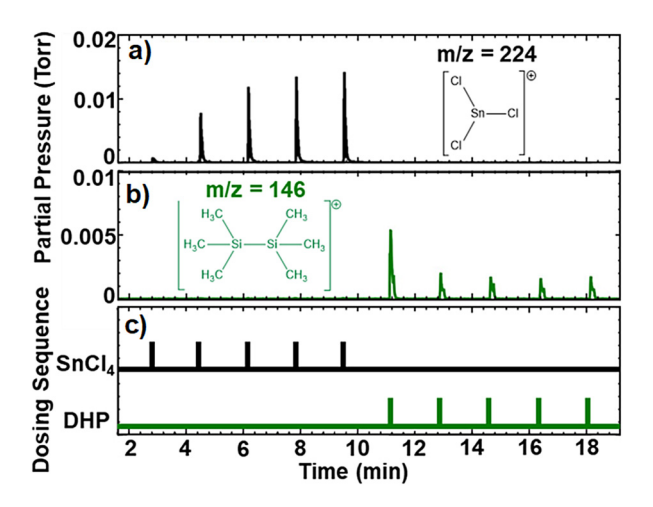


Fig. 10. QMS data during $SnCl_4/DHP$ processing at 190 °C on Si substrates for 5 subdoses of $SnCl_4$ followed by 5 subdoses of DHP, separated by N_2 purges. Most prominent mass fragments (a) m/z 224 (black) and (b) 146 (green) shown with their respective predicted structures. (c) $SnCl_4/DHP$ dosing sequence corresponding to the QMS data in (a) and (b).

IV. DISCUSSION

A. Proposed SnCl₄/DHP reaction mechanism

Based on the observed growth rate and the *in situ* mass spectroscopy results, Sn ALD using SnCl₄ and DHP was hypothesized to proceed via the reaction scheme in Fig. 11.

During steady-state ALD, the SnCl₄ is anticipated to adsorb on the chlorinated surface, possibly through electrostatic interactions between the electron-rich metal surface and the SnCl₄. During the DHP exposure step, available Cl species promote cleavage of Si–N bonds in the DHP, forming gas-phase trimethylchlorosilane (containing thermodynamically favored Si–Cl bonds) and heterocyclic aromatic pyrazine. The abstraction of surface Cl by trimethylsilane donates an electron to the surface to form a Sn–Sn bond. Subsequent formation of Sn–Sn bonds is expected to occur until all DHP is consumed or the surface Cl species are not accessible to the DHP molecule. Sections IV A 1 and IV A 2 describe the how each key step in this process relates to the observed experimental results.

1. SnCl₄ adsorption

The QCM results in Figs. 2 and 3 show mass gain upon SnCl₄ exposure step during steady-state growth, consistent with adsorption of the metal halide precursor. Within the ALD window (i.e., at 190 °C used for QCM), the mass uptake saturates after the first 2 s SnCl₄ subdose. Likewise, the *in situ* QMS results in Fig. 10 are consistent with consumption of the SnCl₄ precursor during the first subdose step. The SnCl₄ adsorption step within the ALD window is consistent with models of other reactant systems during ALD,^{29,30} including, for example, redox active Cu(II) precursor dissociation during Cu ALD.³¹

2. DHP desilylation and pyrazine elimination

QCM results in Figs. 2 and 3 show mass loss during DHP exposure, which we ascribe to the loss of surface Cl forming

Sn–Sn bonds and volatile trimethyl chlorosilane and pyrazine, as shown in Fig. 11. The XPS results in Table I show a decrease in Cl impurities with increased temperature, indicating more efficient removal of Cl by DHP at elevated deposition temperatures. Klesko *et al.* ¹⁵ hypothesized that since the proposed DHP intermediate ring structure is antiaromatic (i.e., $8\pi \ e^-$ in the ring structure), the driving force for the metallic surface reduction lies in the negative reduction potential of the DHP dianion ($E_{1/2} = -2.32 \ V$ versus ferrocene) formed during the desilylation process.

In Fig. 10(b), the peak at m/z = 146 was relatively large during the first subdose and decreased to saturation during subsequent subdosing. This result indicates that m/z = 146 appears as a fragment of the unreacted DHP precursor [see Fig. 9(b)] and as by-product of the SnCl₄/DHP process. Since this species was detected in a greater concentration after reaction, its formation is likely a result of downstream reactions, or possibly during the chemical cracking at the QMS filament, of TMS-Cl and unreacted or partially reacted DHP species. The large concentration of gas-phase products during the first DHP dose followed by saturation is consistent with QCM results in Fig. 3(b), where a single DHP subdose is sufficient to reduce the surface.

As shown in Fig. 11, the lone pair electrons on the nitro group of the as formed pyrazine by-product provide weak Lewis base sites that may promote surface re-adsorption on the electron-rich metallic surface. The QCM results in Fig. 3 show a net mass loss during DHP dosing at both low and high temperatures, indicating that surface adsorption is sufficiently weak, and yet likely temperature dependent, to allow pyrazine to be removed during N_2 purging.

B. Growth saturation

The QCM results in Figs. 3 and 4, along with the QMS data in Fig. 10, give evidence for reaction saturation during the SnCl₄ and DHP dose sequences. For both reactants, multiple subdoses show decreasing mass uptake as dose

Fig. 11. Proposed reaction mechanism between DHP and two surface-bound SnCl_x species. (1) SnCl₄ exposure and subsequent densification gives a Sn–Cl surface. (2) DHP is exposed to the Sn–Cl surface, breaking Si–N bonds on the DHP to give off TMS-Cl by-products. (3) Intermediate ring structure which can donate electrons to create a Sn–Sn bond and eliminate pyrazine. (4) One Sn–Sn bond formed per DHP molecule.

proceeds. As shown in Fig. 4, QCM results reveal a constant mass uptake of ~250 ng cm⁻² cycle⁻¹, corresponding to ~0.9 monolayer cycle⁻¹. The results in Fig. 4 show consistent mass uptake versus temperature, indicating an effective ALD window from 170 up to 210 °C, the maximum temperature studied.

For substrate temperatures less than 170 °C (i.e., below the ALD window), QCM results in Figs. 2-4 show significantly larger net mass uptake during the SnCl₄/DHP dose sequence, especially after extended film growth. The large mass uptake is consistent with the formation of particles on Au-coated QCM substrates (Fig. 5), giving rise to net large surface areas. Large agglomeration of Sn metal has been previously observed during thin film deposition. 32,33 For example, Sn films deposited by CVD using Sn [N(SiCH₃)₂]₂ on HF-dipped Si substrates at 350 °C resulted in thick films with the top surface covered with Sn spheres 500 nm-7.5 μ m in diameter. ³² According to Wang et al., ³³ epitaxial growth of Sn metal on Si substrates revealed Sn island growth with continuous layers between islands. This is an example of Stranski-Krastanov growth, where the formation of islands occurs in order to reduce the crystal strain energy.³⁴

In addition, unpolished QCM crystals were previously shown to have at least 16% larger surface area than the geometric surface area (assuming a planar substrate).³⁵ Rough QCM deposition surfaces, seen in Fig. 5(b), would result in a larger area for reaction and therefore an overestimation of net mass gain per unit area per cycle observed by QCM.^{35–38} A 16% increase in active surface area would correspond to a decrease in GPC at 190 °C from 2.7 Å cycle⁻¹ (0.9 monolayer cycle⁻¹) to 2.3 Å cycle⁻¹ (0.77 monolayer cycle⁻¹).

C. Film composition

ToF-SIMS (Fig. 7) and XPS (Fig. 8) data confirm the presence of Sn metal for films deposited at 190 °C, with an interfacial SnO₂/SiO₂ layer between the Si and Sn. The maxima of the SnO₂ and SiO₂ peaks in Fig. 7(b) occur at nearly the same sputtering times as the corresponding CN and ³⁷Cl maxima, which may be due to incomplete surface reactions, leaving behind a small amount (2–4 at. %) of C, N, and Cl impurities. This implies that the Sn film has a higher impurity concentration near the oxide interface but decreases as the film thickness increases.

V. SUMMARY AND CONCLUSIONS

This work demonstrated the first thermal ALD process for depositing Sn metal from SnCl₄ and DHP. ALD process parameters were determined, such as an ALD window between 170 and 210 °C (maximum temperature tested), saturated linear mass uptake (~250 ng cm⁻² cycle⁻¹), a growth rate of ~0.3 Å cycle⁻¹, and good thickness uniformity over tens of micrometers. An oxidation/reduction mechanism was proposed for the DHP and SnCl₄ system. First, SnCl₄ densified on the substrate followed by an exposure of the DHP reducing agent. The DHP underwent a desilylation

process, removing Cl groups from the surface-bound Sn-Cl, giving off volatile TMS-Cl and forming an intermediate DHP ring structure. The intermediate species, which is an antiaromatic ring structure, donates electrons to form a Sn-Sn bond and eliminate as aromatic pyrazine.

This mechanism was tested using *in situ* QCM and QMS experiments. Within the ALD window, the SnCl₄ appeared to densify on the starting surface leading to a mass increase, and saturated after 1–2 consecutive subdoses. No other reactants or products were observed during SnCl₄ dosing, confirming SnCl₄ adsorption and surface densification. DHP subdoses also revealed saturated reaction conditions, with a net mass loss being observed, indicative of Cl removal via TMS-Cl by-products. Since a net mass loss was observed for the DHP dose, it can be assumed that the intermediate species are removed before the subsequent SnCl₄ dose and most likely eliminated as pyrazine. At temperatures below the ALD window, desorption of excess SnCl₄ was slower than at higher temperature.

The film purity of the deposited films was analyzed using ToF-SIMS and XPS. A lower concentration of C, N, and Cl impurities was observed for Sn films deposited at 190 °C (3 at. % C, 4 at. % N, and 2 at. % Cl) compared to those at 130 °C (5 at. % C, 9 at. % N, and 13 at. % Cl). At low temperature, the higher impurity percentages are most likely due to incomplete SnCl₄ desorption, which then introduces steric hindrance effects for Cl removal by DHP. Furthermore, the aromatic pyrazine molecule produced during the elimination process is a weak Lewis base, which may lead to further incorporation into the film at lower temperatures. The oxidation/reduction chemistry presented here may be applied to other metal precursors and may increase the applicability of metal ALD for a variety of purposes.

ACKNOWLEDGMENTS

The authors acknowledge the financial support from the National Science Foundation (NSF Award No. 1704151) and the National Defense Science and Engineering Fellowship Program. The authors would like to acknowledge EMD performance materials for their support and helpful discussions of results. Acknowledgement is also due to the Analytical Instrumentation Facility (AIF) at North Carolina State University, which is supported by the State of North Carolina and the National Science Foundation, and Duke's Shared Materials Instrumentation Facility.

- ⁵A. Anani, S. Crouch-Baker, and R. A. Huggins, J. Electrochem. Soc. **134**, 3098 (1987).
- ⁶J. Li, A. K. Dozier, Y. Li, F. Yang, and Y.-T. Cheng, J. Electrochem. Soc. **158**, A689 (2011).
- ⁷Z. Liu, B. Deng, G. J. Cheng, H. Deng, and P. P. Mukherjee, J. Appl. Phys. **117**, 214301 (2015).
- ⁸M. Alaf, D. Gultekin, and H. Akbulut, Acta Phys. Pol. A **123**, 323 (2013).
- ⁹J. Han *et al.*, Nat. Commun. **9**, 402 (2018).
- ¹⁰J. B. Goodenough and Y. Kim, Chem. Mater. **22**, 587 (2010).
- ¹¹K. Ui, S. Kikuchi, Y. Kadoma, N. Kumagai, and S. Ito, J. Power Sources 189, 224 (2009).
- ¹²R. Z. Hu, M. Q. Zeng, and M. Zhu, Electrochim. Acta **54**, 2843 (2009).
- ¹³T. S. Arthur et al., MRS Bull. **36**, 523 (2011).
- ¹⁴T. Saito, H. Nishiyama, H. Tanahashi, K. Kawakita, H. Tsurugi, and K. Mashima, J. Am. Chem. Soc. **136**, 5161 (2014).
- ¹⁵J. P. Klesko, C. M. Thrush, and C. H. Winter, Chem. Mater. 27, 4918 (2015).
- ¹⁶W. M. Haynes, *Handbook of Chemistry and Physics*, 96th ed. (CRC Press, 2015).
- ¹⁷Tin (IV) Chloride (Anhydrous); International Chemical Safety Card No. 0953 (U.S. National Version) (National Institute for Occupational Safety and Health, Centers for Disease Control and Prevention, Atlanta, GA, 2017). See http://www.cdc.gov/niosh/ipcsneng/nen.
- ¹⁸D. V. Nazarov, N. P. Bobrysheva, O. M. Osmolovskaya, M. G. Osmolovsky, and V. M. Smirnov, Rev. Adv. Mater. Sci. 40, 262 (2015).
- ¹⁹J. Musschoot, Q. Xie, D. Deduytsche, S. Van den Berghe, R. L. Van Meirhaeghe, and C. Detavernier, Microelectron. Eng. 86, 72 (2009).
- ²⁰S. E. Atanasov, B. Kalanyan, and G. N. Parsons, J. Vac. Sci. Technol. A 34, 01A148 (2016).
- ²¹V. R. Anderson, A. S. Cavanagh, A. I. Abdulagatov, Z. M. Gibbs, and S. M. George, J. Vac. Sci. Technol. A 32, 01A114 (2014).
- ²²J. W. Elam, M. Schuisky, J. D. Ferguson, and S. M. George, Thin Solid Films 436, 145 (2003).
- ²³E. Levrau, K. Devloo-Casier, J. Dendooven, K. F. Ludwig, P. Verdonck, J. Meersschaut, M. R. Baklanov, and C. Detavernier, Langmuir 29, 12284 (2013).
- ²⁴T. Abell, J. Schuhmacher, Z. Tokei, Y. Travaly, and K. Maex, Microelectron. Eng. 82, 411 (2005).
- ²⁵S. K. Karuturi, L. Liu, L. T. Su, Y. Zhao, H. J. Fan, X. Ge, S. He, and A. T. I. Yoong, J. Phys. Chem. C 114, 14843 (2010).
- ²⁶Y. Liu, M. Gibbs, C. L. Perkins, J. Tolentino, M. H. Zarghami, J. Bustamante, and M. Law, Nano Lett. 11, 5349 (2011).
- ²⁷P. Linstrom and W. G. Mallard, NIST Chemistry WebBook, NIST Standard Reference Database Number 69 (National Institute of Standards and Technology, Gaithersburg, MD, 2015)
- ²⁸NIST X-Ray Photoelectron Spectroscopy Database, Version 4.1, (National Institute of Standards and Technology, Gaithersburg, MD, 2018).
- ²⁹L. L. Yusup, J.-M. Park, Y.-H. Noh, S.-J. Kim, W.-J. Lee, S. Park, and Y.-K. Kwon, RSC Adv. 6, 68515 (2016).
- ³⁰Q. M. Phung, G. Pourtois, J. Swerts, K. Pierloot, and A. Delabie, J. Phys. Chem. C 119, 6592 (2015).
- ³¹G. Dey and S. D. Elliot, J. Phys. Chem. C **119**, 5914 (2015).
- ³²D. V. Baxter, M. H. Chisholm, G. J. Gama, A. L. Hector, and I. P. Parkin, Chem. Vap. Depos. 1, 49 (1995).
- ³³L. L. Wang, X. C. Ma, S. H. Ji, Y. S. Fu, Q. T. Shen, J. F. Jia, K. F. Kelly, and Q. K. Xue, Phys. Rev. B: Condens. Matter Mater. Phys. 77, 205410 (2008)
- ³⁴A. Baskaran and P. Smereka, J. Appl. Phys. **111**, 044321 (2012).
- ³⁵J. W. Elam, M. D. Groner, and S. M. George, Rev. Sci. Instrum. **73**, 2981 (2002).
- ³⁶K. Rechendorff, M. B. Hovgaard, M. Foss, and F. Besenbacher, J. Appl. Phys. **101**, 114502 (2007).
- ³⁷L. Daikhin and M. Urbakh, Faraday Discuss. **107**, 27 (1997).
- ³⁸E. B. Yousfi, J. Fouache, and D. Lincot, Appl. Surf. Sci. 153, 223 (2000).

¹L. Ansari, G. Fagas, J. P. Colinge, and J. C. Greer, Nano Lett. **12**, 2222 (2012).

²L. Ansari, G. Fagas, and J. C. Greer, Appl. Phys. Lett. **105**, 123105 (2014).

³J. M. Whiteley, J. W. Kim, C. S. Kang, J. S. Cho, K. H. Oh, and S.-H. Lee, J. Electrochem. Soc. **162**, 711 (2015).

⁴G. R. Goward, N. J. Taylor, D. C. S. Souza, and L. F. Nazar, J. Alloys Compd. 329, 82 (2001).